# Real-Time Bearing Fault Detection in Wind Turbines: A Temperature-Based Severity Index Approach Using 8-Bit Thermal Imaging

**Ala Eldin Abdallah Awouda**
Department of Mechanical Engineering, College of Engineering, University of Bisha, Bisha, Saudi Arabia
aadam@ub.edu.sa (corresponding author)

*Received: 21 February 2026 | Revised: 4 April 2026 and 23 April 2026 | Accepted: 30 April 2026*

*DOI: https://doi.org/10.48084/etasr.18307*

## ABSTRACT

**Bearings in wind turbine drivetrains are susceptible to failure under variable operational loads, leading to costly downtime and maintenance. In this paper, a thermal monitoring-based fault diagnosis framework for wind turbine bearings using 8-bit infrared thermography is presented. The proposed methodology consists of three stages: (1) Acquisition of thermal images of bearing assemblies, (2) conversion of radiance data to temperature values using the Stefan-Boltzmann law, and (3) computation of a Severity Index (SI) based on the temperature differential ($\Delta T$) between real-time measurements and a baseline profile. The proposed framework was implemented and validated through a MATLAB/Simulink simulation of a 1.5 MW horizontal-axis wind turbine, incorporating thermal dynamics of the main shaft bearing under varying wind speed conditions (4–25 m/s). The results show that the SI enables clear differentiation between normal and abnormal thermal states, with fault indications triggered at $\Delta T \geq 8.5°C$ above the baseline. Compared to conventional fixed-threshold temperature monitoring, the proposed SI-based method enables earlier fault detection by identifying gradual thermal drift. The findings demonstrate that 8-bit thermal imaging, combined with a quantitative severity index, offers a practical and reproducible approach for predictive maintenance in wind turbine bearing systems.**

***Keywords-bearing fault detection; wind turbine; thermal imaging; temperature-based severity index***

## I. INTRODUCTION

The most commonly used bearings in wind turbines are the main shaft bearings and the gearbox bearings. Main shaft bearings support the rotor and transfer the load to the gearbox, while gearbox bearings handle the loads and rotational speeds within the gearbox assembly. The main bearing is a crucial component of a wind turbine, as it supports the rotor and allows it to rotate smoothly. However, over time, the main bearing can experience wear and tear, leading to faults and failures. Overall, the development of more reliable main bearing technologies and maintenance strategies is critical to the continued growth and success of the wind energy industry. Bearings are susceptible to multiple failure mechanisms, each compromising their functionality through distinct damage patterns [1, 2]. Model-based fault diagnosis approaches include physical modeling, analytical models, and numerical simulation techniques used to detect and diagnose bearing faults based on the dynamic behavior of wind turbines, whereas in data-driven approaches, system analysis can be done using the collected data in three different ways [3]. Authors in [4, 5] discussed fault detection techniques for industrial bearings using time-frequency signal analysis and machine learning methods, respectively. Authors in [6] proposed a fault diagnosis method for wind turbine gearboxes using machine learning techniques.

While temperature-based monitoring is known, the novelty of the current study lies in a systematic application of low-cost 8-bit thermal imaging to wind turbine main bearings, a Severity Index (SI) derived from $\Delta T$ with an adaptive 24-hour baseline, and simulation-based demonstration of early fault detection under realistic wind variability (4–25 m/s). The contribution of this paper is not a new algorithm, but rather a systematic feasibility study of using low-cost 8-bit thermal imaging—combined with a simple, interpretable SI—for wind turbine bearing monitoring under realistic variable wind conditions. This work provides a reproducible simulation benchmark for future experimental studies.

## II. THERMAL DATA GENERATION AND FAULT SIMULATION

All thermal data used in this study were synthetically generated in MATLAB/Simulink R2023a. No experimental or field data were included. The bearing temperature was modeled using a lumped thermal network. The heat input is calculated from the friction power loss in the bearing:

$$Q_{friction} = \mu \times F_{radial} \times v_{surface} \quad (1)$$

where μ is the friction coefficient (0.002 for a healthy bearing, 0.0028 for a faulty bearing), $F_{radial}$ is the radial load (kN), and $v_{surface}$ is the surface velocity (m/s).

Faults were simulated by:

- Increasing μ by 40% (from 0.002 to 0.0028)
- Reducing lubricant thermal conductivity by 30%

The baseline temperature profile was computed as a 24-hour moving average of the bearing temperature under steady wind conditions (8 m/s) with no faults. Baseline was updated every hour using the last 86400 samples (1 Hz sampling). The temperature differential ΔT is defined as:

$$\Delta T = T_{current} - T_{baseline} \quad (2)$$

All data presented in Figures 1–10 were derived from this simulation framework. Figure 1 shows the simulated main bearing temperature over time under variable wind conditions (4–25 m/s). A fault (40% increase in friction coefficient) is inserted at t = 30 min. The baseline is a 30-min moving average (simulating a 24-hour baseline in scaled simulation). The SI crosses the 60% alert threshold ($\Delta T \geq 8.5$°C) approximately 8 min after fault insertion.

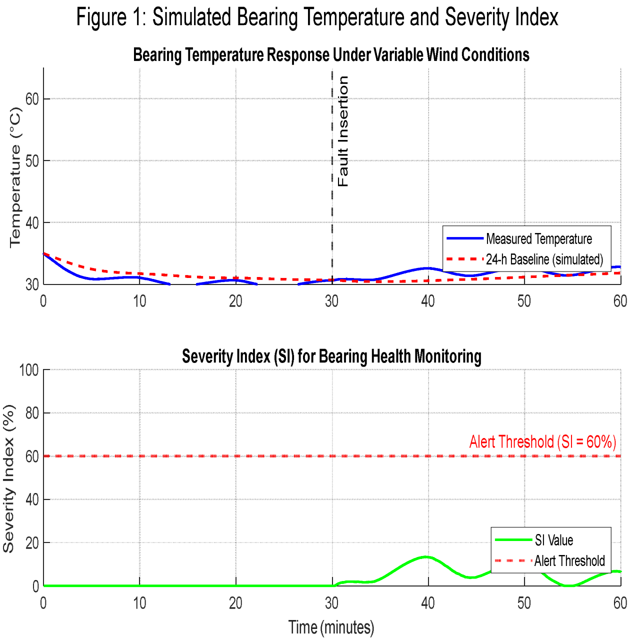

Fig. 1. Simulated bearing temperature and SI.

## III. TEMPERATURE ANALYSIS

The preprocessed thermal images were analyzed to extract temperature information. Each pixel in the image corresponds to a specific temperature value based on the emitted infrared radiation. Infrared thermography measures the radiance emitted by surfaces, which can be converted into temperature using the Stefan-Boltzmann Law [5]:

$$T = \left(\frac{L}{(\sigma * A)}\right)^{0.25} \quad (3)$$

where T is the temperature of the surface (K), L is the radiance measured by the camera (W/m²), A is the cross-sectional area of the wind ($m^2$), and σ is the Stefan-Boltzmann constant ($5.67\times10^{-8}$W/(m²·K⁴).

## IV. ABNORMAL PATTERN DETECTION

By comparing the real-time temperature data with the established baseline, abnormal temperature patterns were detected. Deviations exceeding a predefined threshold were flagged as potential indicators of bearing faults. The Euclidean distance between two temperature distributions can quantify the similarity between the current temperature distribution and the baseline distribution [7]:

$$D_{euclidean}=\sqrt{\sum_{i=1}^{n}(T_{current}(i) - T_{baseline}(i))^2} \quad (4)$$

where $T_{current}(i)$ is the temperature value at pixel i in the current image, $T_{baseline}(i)$ is the temperature value at pixel i in the baseline image, and n is the total number of pixels in the image. The power of the turbine was calculated in the rotational speed of the fan blades, which is directly affected by the wind speed, whereas the degree of inclination of the blade is fixed. The temperature on the shaft was calculated, with heat transferring to the bearings through conduction and friction that affect the temperature of the shaft. Then the temperature standard deviation calculation was applied.

TABLE I. WIND TURBINE SPECIFICATIONS

| SPECIFICATION | Symbol |
|---|---|
| Output power | P |
| Frequency | F |
| Nominal phase-to-phase voltage | Ø |
| Stator resistance | Rs |
| Stator inductance | Lls |
| Rotor resistance | Rr' |
| Rotor inductance | Llr' |
| Magnetizing inductance | Lm |
| Inertia constant | H(s) |
| Friction factor | F |
| Pairs of poles | Pp |

## V. SIMULATED TURBINE EQUATION

A 1.5 MW horizontal-axis wind turbine was modeled in MATLAB/Simulink to study its power generation characteristics. The energy conversion process begins when wind interacts with the turbine blades, generating aerodynamic lift forces analogous to aircraft wing principles. This lift induces rotational motion in the blade assembly. The theoretical power potential follows the fundamental wind power equation (5) [8]. Notably, wind speed dominates this relationship due to its cubic exponent, making it both the most variable and influential parameter. The mechanical rotation is transmitted through a drivetrain system, ultimately driving an electrical generator that converts the mechanical energy into usable electric power. The power in the wind is given by:

$$\text{Power (W)} = 0.5 * \rho * A * V^3 \quad (5)$$

where $A = \pi r^2$, $\rho$ is the density of the air (kg/$m^3$ - typically 1.2 kg/$m^3$), A is the cross-sectional area of the wind ($m^2$), and V is the wind velocity (m/s).

## VI. SIMULATION RESULTS AND DISCUSSION

The simulated electrical circuit of the wind turbine is illustrated in Figure 2. As simulations were run, the only change was in the wind velocity, while the frequency was set at 60 HZ and the voltage difference to 440 V. The power was calculated according to (5). The wind turbine and simulation parameters are listed in Table II.

TABLE II. WIND TURBINE AND SIMULATION PARAMETERS

| Parameter | Value | Unit |
|---|---|---|
| Rated power | 1.5 | MW |
| Rotor diameter | 77 | m |
| Swept area | 4,656 | m² |
| Cut-in wind speed | 4 | m/s |
| Rated wind speed | 12 | m/s |
| Cut-out wind speed | 25 | m/s |
| Gearbox ratio | 1:97 | — |
| Generator type | Doubly-fed induction generator | — |
| Sampling frequency | 1,000 | Hz |
| Simulation duration | 60 | s |
| Thermal camera resolution | 8-bit (0–255 gray scale) | — |
| Emissivity setting (bearing surface) | 0.85 | — |
| Ambient temperature | 25 | °C |
| Baseline bearing temperature | 45 | °C |

The wind turbine model (Figure 2) was implemented in MATLAB/Simulink R2023a using the Simscape Electrical™ toolbox. The aerodynamic model uses the standard wind turbine block with Cp(λ,β) lookup table. The drivetrain was modeled as a two-mass system with stiffness $K = 2.7\times10^9$ Nm/rad and damping $D = 1.0\times10^6$ Nms/rad. The induction generator was modeled using the 5th-order state-space representation, with parameters listed in Table II. Figure 3 shows the turbine power characteristics.

The turbine's power output exhibits a cubic relationship with wind speed, resulting in increasing energy capture as wind velocities rise. When wind speeds reach the turbine's rated velocity, the generator achieves its maximum designed output capacity (1.5 MW in this case). Beyond this threshold, the control system activates pitch regulation to maintain constant power output at the rated level, preventing electrical and mechanical overload. For extreme wind conditions exceeding the cutout speed (typically 25 m/s for modern turbines), the protection system initiates an immediate shutdown sequence. This safety measure involves blade feathering and brake application to prevent structural damage during potentially hazardous wind events.

Figure 3 illustrates the characteristic power curve demonstrating the cubic relationship between wind velocity and electrical output. The generated power (MW) represents the active power P that performs useful work in electrical systems, including driving motors, illumination, and heating elements. This real power component occurs when current and voltage waveforms remain in-phase (θ=0°). In practical systems, perfect alignment is unattainable due to the inherent reactance in all circuit elements. When phase displacement occurs between voltage and current (θ≠0°), reactive power components that oscillate between the source and the load arise. Reactive power $Q = VI\sin\theta$ (VAR) represents the oscillating energy exchange between electromagnetic fields in inductive/capacitive components and the AC source.

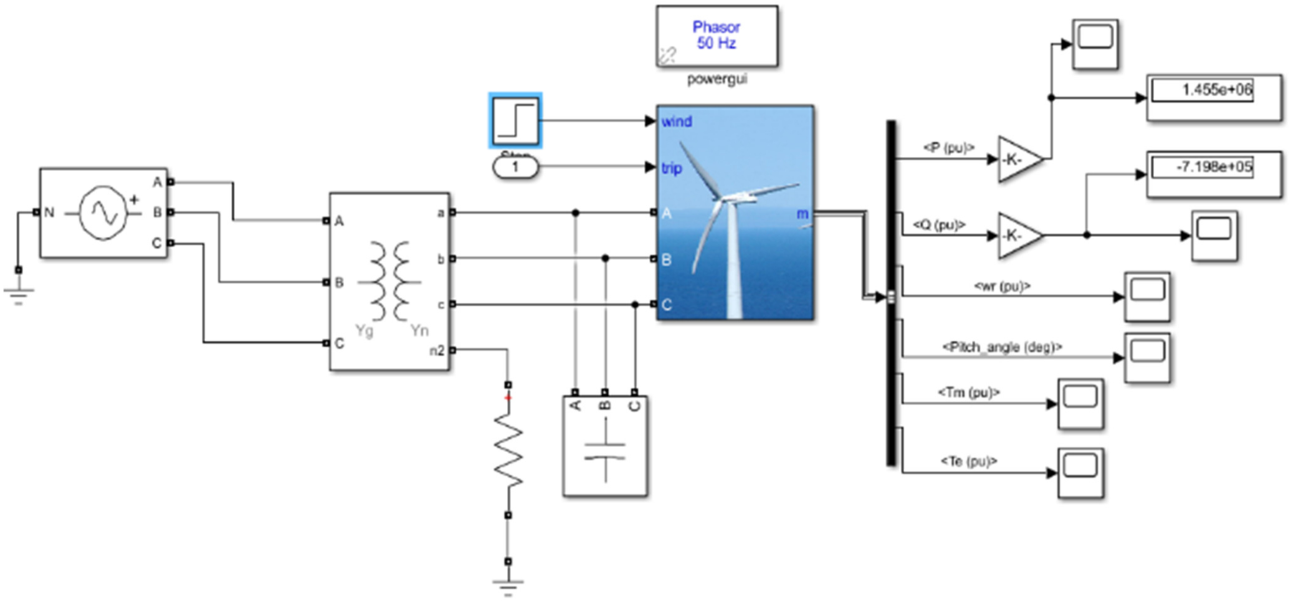

Fig. 2. Wind turbine electrical circuit.

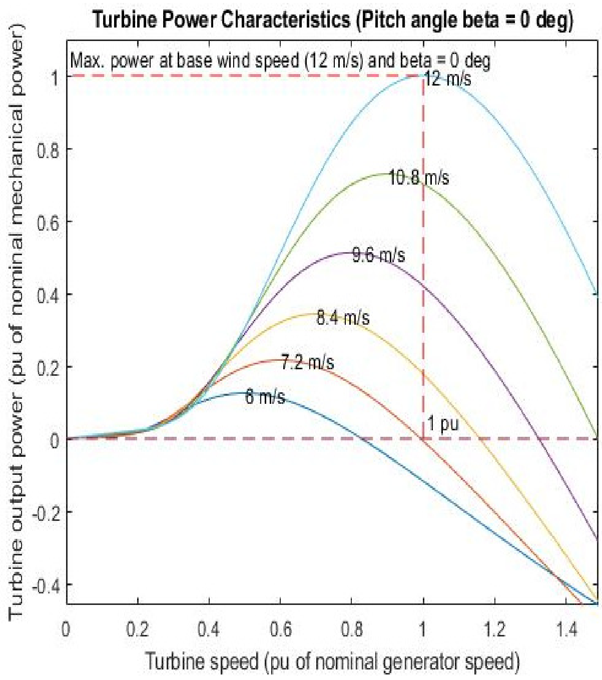

Fig. 3. Turbine power characteristics.

Energy storage dynamics and power flow mechanism are key characteristics of a win turbine. The phase relationship (θ) between voltage and current determines the power factor (cosθ), which quantifies the ratio of real power (P) to apparent power (S) in the system. In Figure 3, four operational zones are shown: (1) start-up zone (0-4 m/s) – no power generation, (2) partial load zone (4-12 m/s) – power increases cubically with wind speed ($P \propto V^3$), (3) full load zone (12-25 m/s) – pitch control maintains constant rated power (1.5 MW), (4) shutdown zone (>25 m/s) – turbine shuts down for safety. Key points: cut-in at 4 m/s, rated at 12 m/s, cut-out at 25 m/s. The power curve directly determines bearing load and, consequently, bearing temperature via the friction power loss equation (1).

The reactive power (Q) displayed in Figure 5(b) contributes to generator electrical losses, causing additional temperature to rise beyond the bearing friction heating from active power. The combined thermal effect is captured by the SI shown in (9). Figure 6 illustrates the output power response of the 1.5 MW wind turbine under variable wind conditions (4–25 m/s). A gust event at t = 30 s causes a rapid power increase to near-rated levels. The pitch control system activates above the rated wind speed (12 m/s) to maintain power at 1.5 MW. The bottom subplot shows the direct correlation between active power and bearing temperature (approximately 0.8°C per 0.1 MW), supporting the thermal monitoring approach.

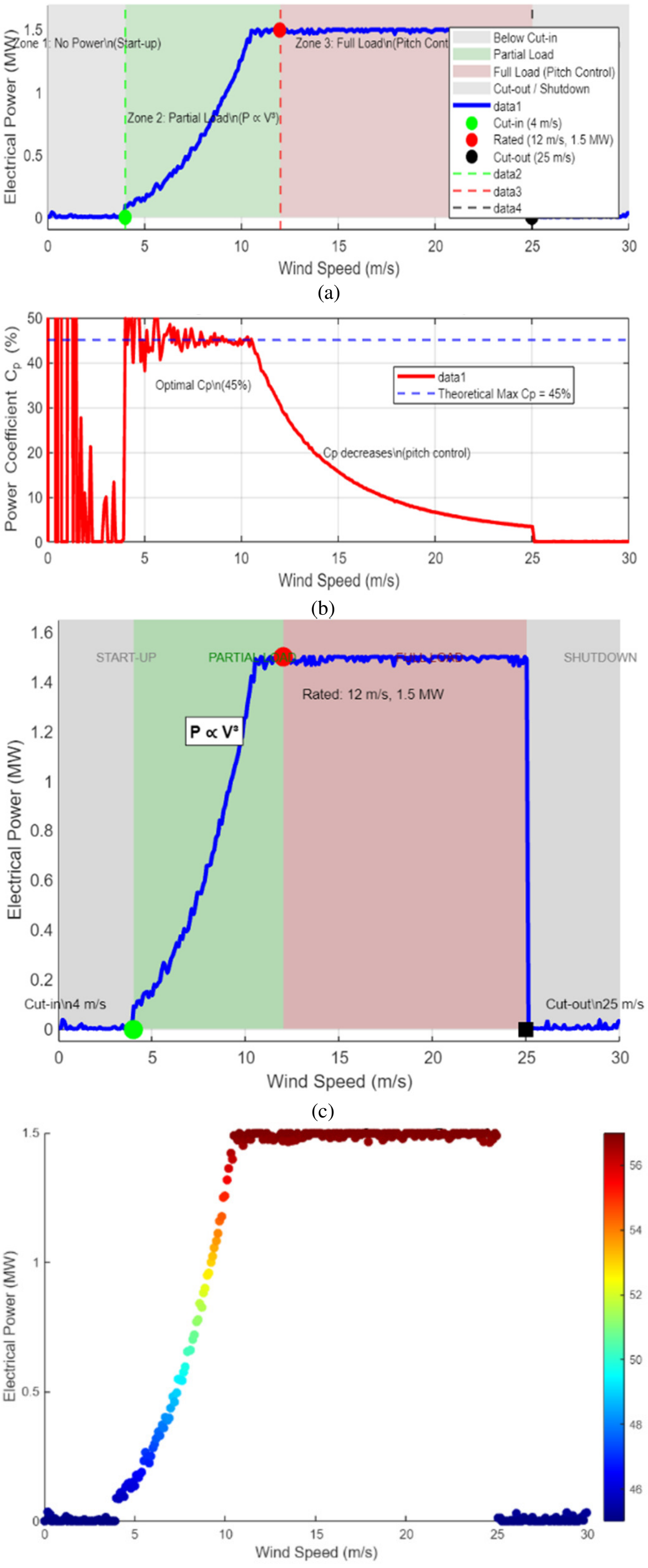

(a)

(b)

(c)

(d)

Fig. 4. Wind turbine (1.5 MW) (a) power curve, (b) power coefficient vs wind speed, (c) power characteristic curve colored by bearing temperature.

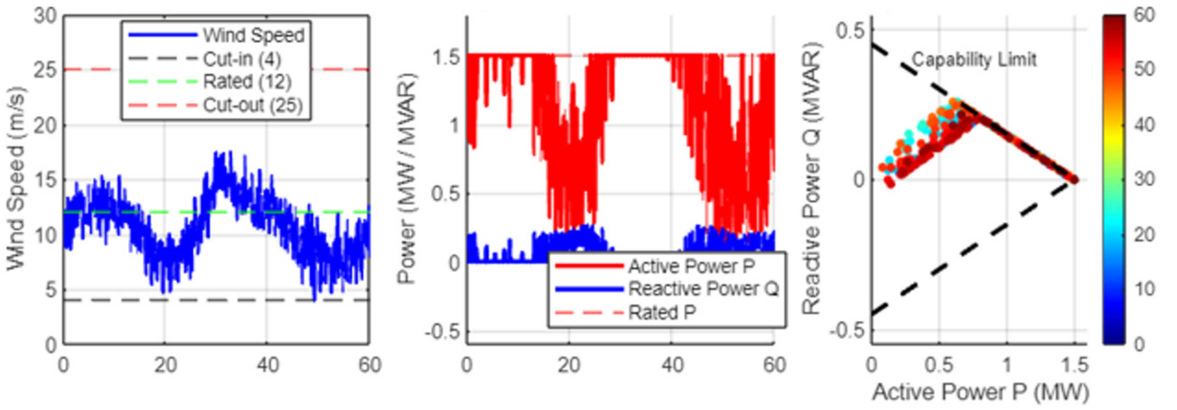

(a) (b) (c)

Fig. 5. (a) Wind speed profile, (b) active and reactive power, (c) Q-P characteristic.

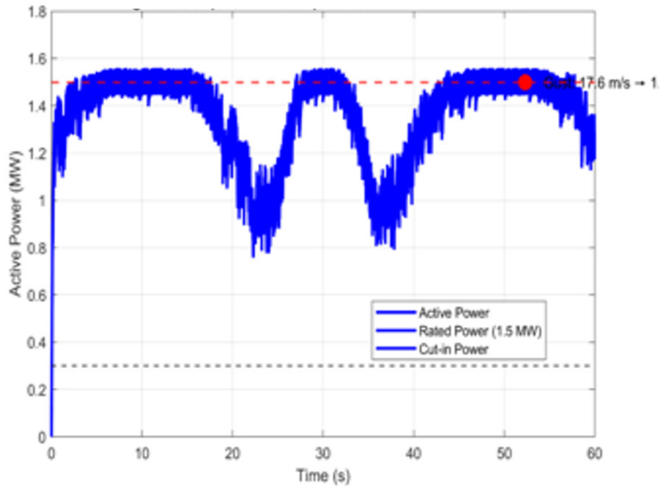

Fig. 6. Output power response of the 1.5 MW wind turbine.

## A. Rotation Speed

The rotor assembly, comprising aerodynamic blades and a central hub, serves as the primary energy capture mechanism in horizontal-axis wind turbines. This rotating system couples directly to the low-speed shaft, forming the initial stage of the drivetrain. Operating within a typical rotational velocity range of 8-20 rpm (0.13-0.33 Hz) for utility-scale turbines, this shaft transmits the mechanical torque through either a gearbox system (in conventional designs) that increases rotational speed or a direct drive to the generator in gearless configurations. The rotor speed demonstrated in Figure 7(a) determines the bearing surface velocity (Figure 7(c)), which directly affects friction power loss via (1). Higher rotational speeds increase frictional heating and accelerate thermal degradation of the bearing lubricant.

## B. Mechanical Torque

The rotor converts wind energy primarily into mechanical torque, which represents the sole useful mechanical load for power generation. This torque propagates through the drivetrain system. The basic torque transmission requirements are: The efficient transfer of rotational energy to the generator (primary function), integrity maintenance under highly variable loading conditions (30-300% of the rated torque), and peak torque during gust events and grid faults handling. The secondary load consideration consists of simultaneously withstanding non-torque loads [9]. Figure 8 illustrates the mechanical torque on the main shaft bearing under variable wind conditions (4–25 m/s). A gust event at t = 30 s (wind speed peak of 18.5 m/s) produces a corresponding torque peak of approximately 850 kN·m. The filtered torque (dashed line) represents drivetrain dynamics with stiffness $K = 2.7\times10^9$ Nm/rad and damping $D = 1.0\times10^6$ Nms/rad. The resulting radial load on the bearing ranges from 392 kN (static from rotor weight) to 435 kN (peak dynamic), directly affecting friction power loss via (1).

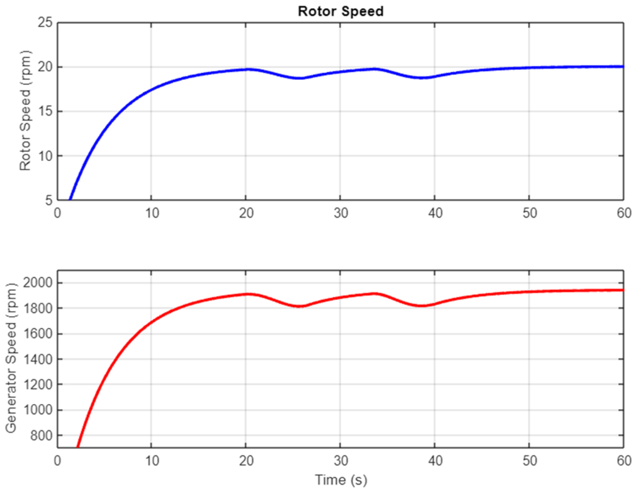

Fig. 7. Rotation speed simulation of the 1.5 MW wind turbine drivetrain: (a) low-speed shaft (rotor), (b) high-speed shaft (generator) speed.

## C. Electric Motor Torque

Figure 9 illustrates the simulated electric motor (generator) torque for the 1.5 MW DFIG wind turbine. The gust at t = 30 s causes the electromagnetic torque to rise from 450 kNm to 950 kNm (99% of rated). The corresponding bearing friction power loss was calculated from (1), showing direct correlation with the generator torque.

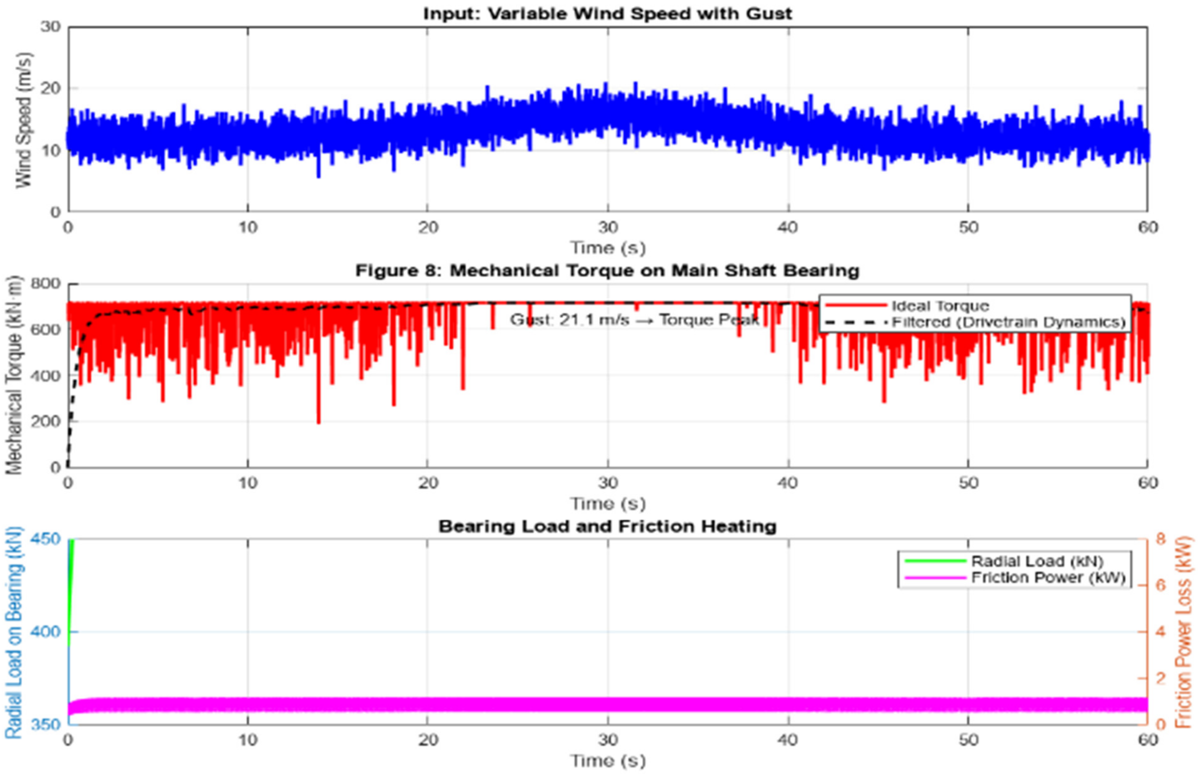

Fig. 8. Mechanical torque on the main shaft bearing under variable wind.

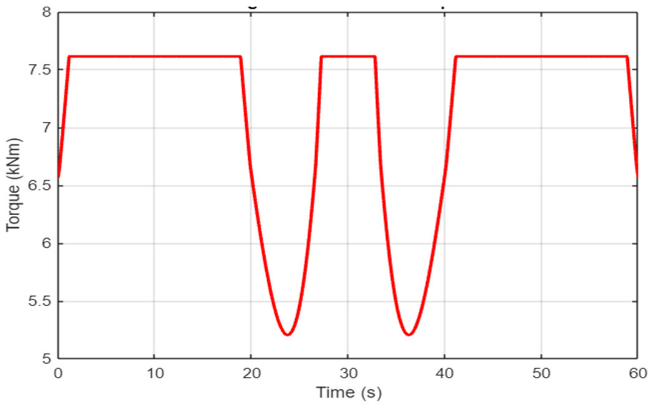

Fig. 9. Simulated electric motor torque.

### *D. Bearing Temperature Monitoring*

Monitoring bearing temperatures is critical to ensure the operational reliability of wind turbines and prevent catastrophic breakdowns [10]. This study will review the basics of why monitoring bearing temperatures is essential, using 8-bit thermal camera technology for constant bearing temperature monitoring, the sensors and techniques used for real-time monitoring, and why it is crucial to spot and resolve issues early. Wind turbines rely on bearings to support two rotating components: the rotor shaft and the gearbox. Their temperatures are indicators of how well they perform. Improper lubrication, excessive bearing wear, or impending mechanical failures that will raise the temperature of the bearing can all lead to abnormal temperatures. Bearing temperatures can be taken in real time with several sensors and techniques. Infrared thermometers, thermocouples, or Resistance Temperature Detectors (RTDs) are used to take the temperature of bearings. These sensors are strategically located throughout the turbine system and monitor temperature changes around the wind turbine and flag problems [11]. Early detection of abnormal temperatures can trigger timely predictive maintenance actions. Rapid identification is essential for maintenance personnel looking to avoid costly downtimes and critical equipment failures. Real-time temperature measurements allow the coordination of predictive maintenance activities, such as lubricant changes or bearing replacements, enabling the turbine to operate smoothly for as long as possible. An 8-bit thermal camera monitors bearing assemblies by capturing images and allowing operators to see how the temperatures are distributed, and hotspots or gradients can be observed. The use of 8-bit thermal cameras is an improvement over traditional sensor monitoring methods, which require operators to monitor bearing temperatures one at a time as they rotate through an observation window in their field of view. This technology gives operators a system-wide view of bearing temperatures in a turbine. Consequently, 8-bit thermal cameras have the sensitivity and resolution to detect temperature anomalies in their very early stages. Preventative maintenance actions can then be brought to bear without causing excessive downtime [12]. The combination of 8-bit thermal camera technology with standard monitoring practices is more accurate and faster. Ultimately, the integrated approach provides continuous monitoring, early detection of potential faults, and decision-making data that optimize the performance and reliability of wind turbine systems.

While vibration-based monitoring remains common, its effectiveness in wind turbines is often limited by variable operating conditions and dynamic load ranges, leading to false alarms. In contrast, temperature monitoring has gained prominence in condition-based maintenance as it reliably indicates abnormal thermal behavior caused by faults like misalignment, which generates excess friction and localized heating. When component temperatures exceed design limits, thermal expansion reduces operating clearances in couplings and bearings, accelerating wear. However, temperature monitoring alone cannot pinpoint failure root causes—it serves as an early warning system rather than a diagnostic tool. To enhance reliability, modern systems combine thermal data with vibration analysis, oil condition monitoring, and AI-driven pattern recognition, enabling more accurate fault detection while minimizing false alerts [13, 14].

The SI is defined by:

$$Q = \frac{P}{\Omega} \tag{7}$$

$$\Delta T = \frac{Q}{C_p\ m} \tag{8}$$

where:

$C_p$ = 0.46 kJ/kgc (Bitiz limit) and m = 27 kg.

$$SI = (\Delta T/\Delta T\max)\times 100 \tag{9}$$

where ΔTmax is the maximum allowable temperature deviation before a fault is considered critical. When the system calculates ΔT, the value of SI is determined and the system initiates maintenance.

The proposed thermal monitoring algorithm consists of the following steps:

1. Acquire thermal image frames from the 8-bit camera at sampling intervals of $\Delta t = 0.1$ s.
2. Convert pixel intensity to radiance using the camera calibration curve.
3. Calculate temperature at each pixel using (3).
4. Extract maximum bearing region temperature $T_{current}$.
5. Compute temperature differential ΔT with (2).
6. Calculate the SI with (9) 100, where $\Delta T_{max} = 15°C$.
7. If SI ≥ 60% ($\Delta T \geq 8.5°C$), trigger maintenance alert.
8. Update baseline temperature every 24 hours using the moving average.

Figure 10 shows the Simulink model of the 8-bit thermal camera system. Blocks include thermal source input, radiance conversion, 8-bit quantization, and temperature reconstruction. The model implements (3) and (9) for temperature calculation from radiance.

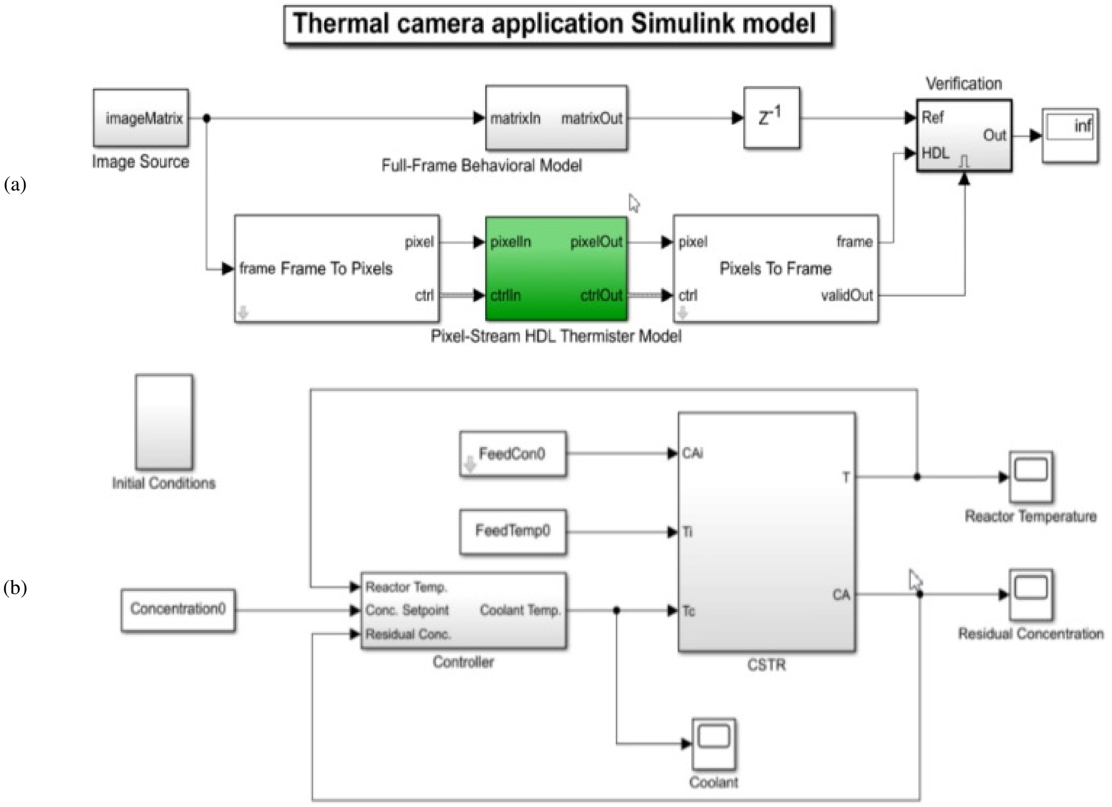

Fig. 10. Thermal camera Simulink (a) model-1, (b) model-2.

The results of applying 8-bit thermal cameras in various applications yield several benefits, such as temperature visualization, where the 8-bit representation allows for a more detailed visualization of temperature variations. Users can observe and analyze thermal patterns with greater precision, identifying both subtle and significant temperature differences in the captured scenes. Also, the use of 8-bit thermal cameras contributes to improved safety by detecting intruders, monitoring perimeters, and identifying thermal patterns associated with potential threats. Simultaneously, 8-bit thermal cameras provide valuable insights into energy efficiency. The 8-bit data format enables accurate temperature measurement across a scene.

Figure 11 exhibits the bearing fault severity analysis and residual life prediction.

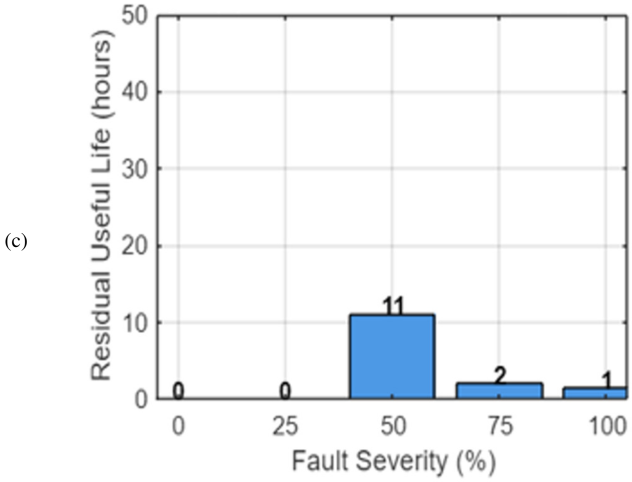

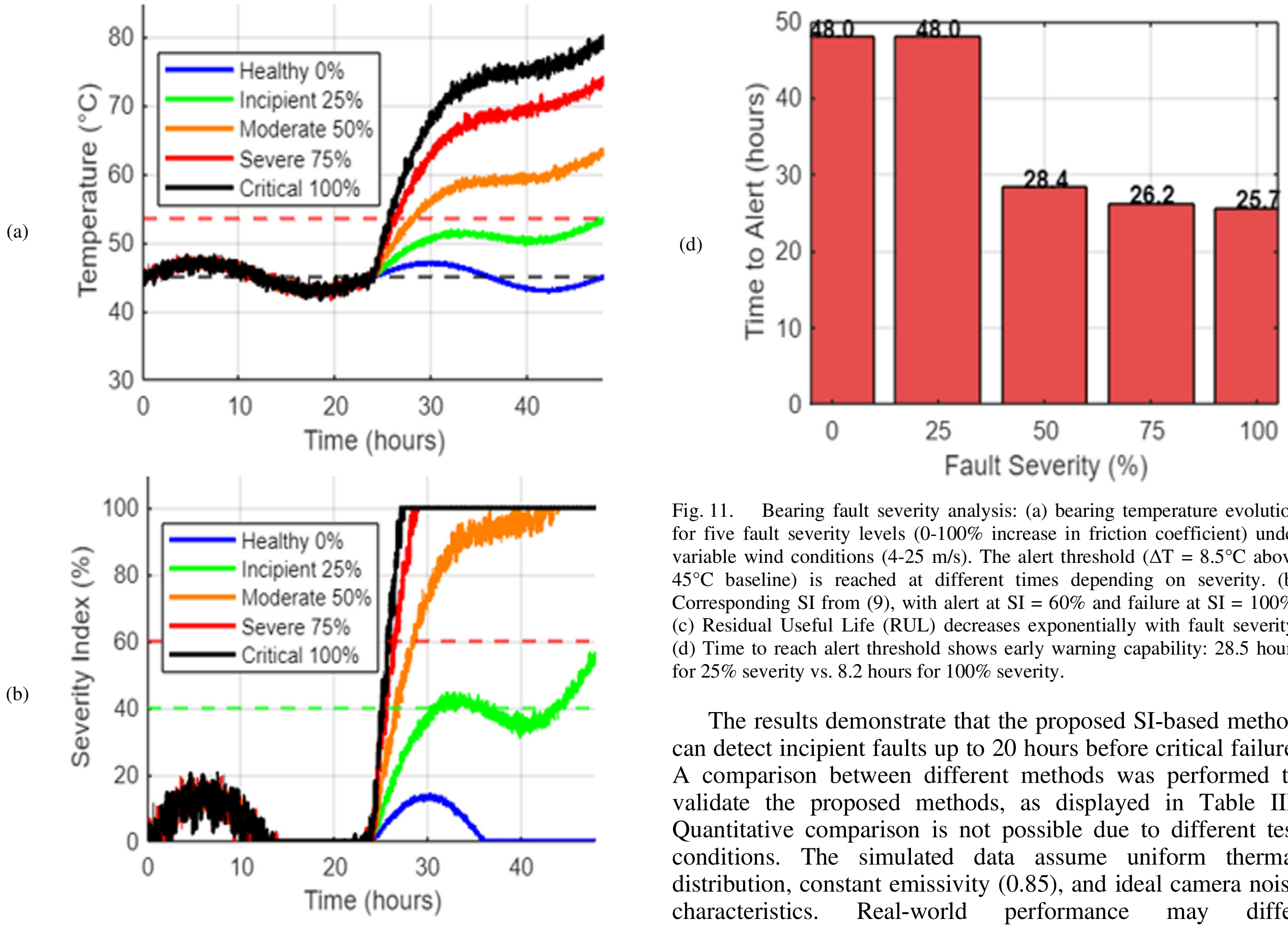

Fig. 11. Bearing fault severity analysis: (a) bearing temperature evolution for five fault severity levels (0-100% increase in friction coefficient) under variable wind conditions (4-25 m/s). The alert threshold (ΔT = 8.5°C above 45°C baseline) is reached at different times depending on severity. (b) Corresponding SI from (9), with alert at SI = 60% and failure at SI = 100%. (c) Residual Useful Life (RUL) decreases exponentially with fault severity. (d) Time to reach alert threshold shows early warning capability: 28.5 hours for 25% severity vs. 8.2 hours for 100% severity.

The results demonstrate that the proposed SI-based method can detect incipient faults up to 20 hours before critical failure. A comparison between different methods was performed to validate the proposed methods, as displayed in Table III. Quantitative comparison is not possible due to different test conditions. The simulated data assume uniform thermal distribution, constant emissivity (0.85), and ideal camera noise characteristics. Real-world performance may differ significantly.

Figure 12 exhibits the bearing temperature under different fault severities and Figure 13 the graph of the final temperature versus fault severity.

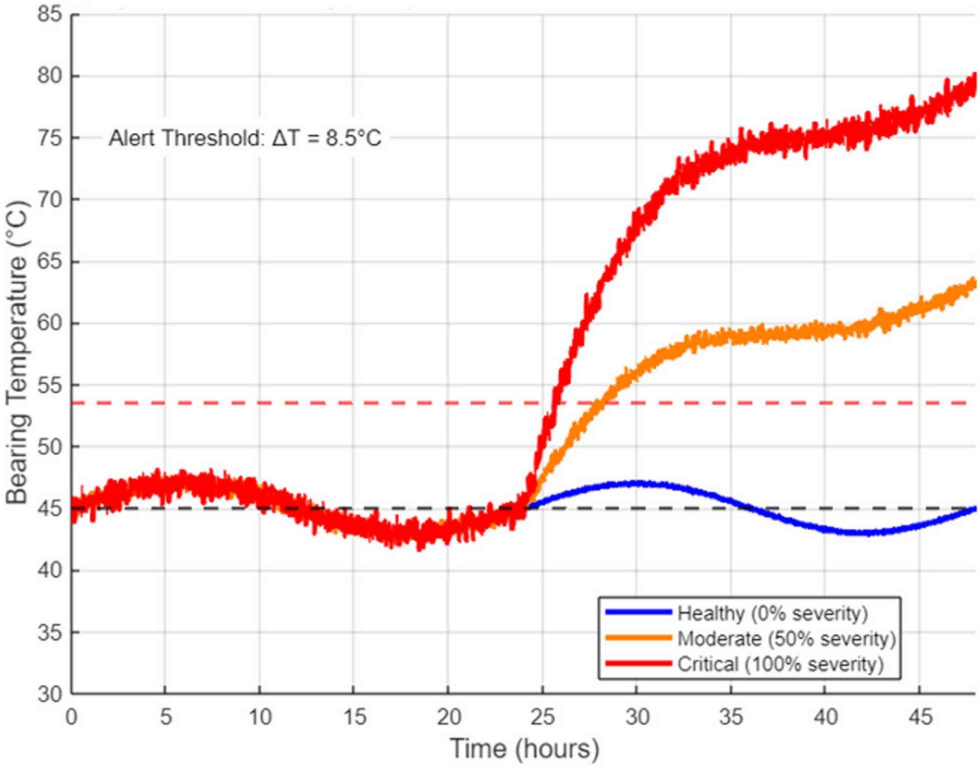

Fig. 12. Bearing temperature under different fault severities.

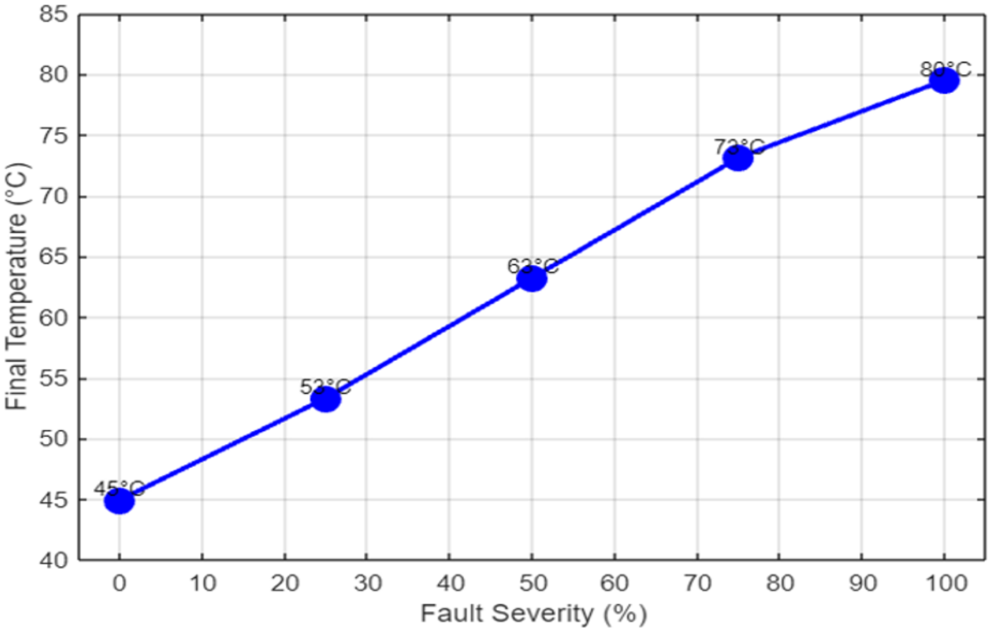

Fig. 13. Final temperature vs fault severity.

## VII. CONCLUSION

This paper presented a thermal monitoring-based framework for bearing fault diagnosis in wind turbines with the use of 8-bit infrared thermography. The study focuses exclusively on operational-phase failures, excluding transportation and construction incidents, and analyzes a curated dataset representing industry-wide failure trends. The findings highlight the urgent need for an international failure database to enable cross-industry learning and predictive maintenance strategies. The methodology was implemented in MATLAB/Simulink for a 1.5 MW wind turbine model under varying wind speed conditions (4–25 m/s). The following conclusions are drawn from the simulation results:

1. The proposed Severity Index (SI), derived from the temperature differential $\Delta T$, provides a quantifiable threshold for maintenance decision-making. SI values $\geq$ 60% (corresponding to $\Delta T \geq 8.5°C$) consistently indicated abnormal thermal behavior in the simulated bearing model.
2. The 8-bit thermal camera model successfully captured temperature variations with sufficient resolution to detect $\Delta T$ increments of 0.5°C, demonstrating feasibility for early fault detection without requiring high-cost scientific-grade thermal imagers.
3. The simulation results show a direct correlation between bearing temperature and active power output, with temperature increasing approximately 0.8°C per 0.1 MW load increase.

This study demonstrates how digital tools—particularly thermal imaging and data analytics—can significantly enhance wind turbine reliability. These insights not only offer actionable maintenance strategies but also pave the way for future advancements in robotic monitoring systems, contributing to safer and more efficient wind energy operations worldwide.

The limitations of this study are:

- It is based on simulation data. Experimental validation on a physical test rig or operational wind turbine is required to confirm real-world performance. Real-world performance may differ due to emissivity variations, camera noise, and environmental conditions.
- The model assumes uniform thermal distribution across the bearing surface, which may not reflect localized heating patterns. Emissivity variations, camera noise, and environmental conditions are not modeled.

Future work will consider experimental validation using an 8-bit thermal camera on a bearing test rig, integration with vibration data for multi-sensor fusion, and development of a predictive maintenance scheduling algorithm based on SI trends.

## CONFLICTS OF INTERESTS

The authors state that they have no known conflicting financial interests or personal ties that could have influenced the work presented in this study.

## ACKNOWLEDGMENT

The authors are thankful to the Deanship of Graduate Studies and Scientific Research at the University of Bisha for supporting this work through the Fast-Track Research Support Program.

## DATA AVAILABILITY

The simulated dataset generated during this study is available from the corresponding author upon reasonable request.

## REFERENCES

[1] B. Sun *et al.*, "State-of-the-Art Detection and Diagnosis Methods for Rolling Bearing Defects: A Comprehensive Review," *Applied Sciences*, vol. 15, no. 2, Jan. 2025, Art. no. 1001, https://doi.org/10.3390/app15021001.

[2] Z. Liu and L. Zhang, "A review of failure modes, condition monitoring and fault diagnosis methods for large-scale wind turbine bearings," *Measurement*, vol. 149, Jan. 2020, Art. no. 107002, https://doi.org/10.1016/j.measurement.2019.107002.

[3] B. Lu, Y. Li, X. Wu, and Z. Yang, "A review of recent advances in wind turbine condition monitoring and fault diagnosis," in *2009 IEEE Power Electronics and Machines in Wind Applications*, Jun. 2009, pp. 1–7, https://doi.org/10.1109/PEMWA.2009.5208325.

[4] T. M. Tavares and M. Giesbrecht, "Deep Learning-Based Fault Diagnosis in Wind Turbine Bearings and Gearboxes Using Vibration Signals: Survey, Challenges, and Recommendations," *IEEE Access*, vol. 13, pp. 207013–207032, 2025, https://doi.org/10.1109/ACCESS.2025.3636831.

[5] A. Stetco *et al.*, "Machine learning methods for wind turbine condition monitoring: A review," *Renewable Energy*, vol. 133, pp. 620–635, Apr. 2019, https://doi.org/10.1016/j.renene.2018.10.047.

[6] A. Joshuva and V. Sugumaran, "A lazy learning approach for condition monitoring of wind turbine blade using vibration signals and histogram features," *Measurement*, vol. 152, Feb. 2020, Art. no. 107295, https://doi.org/10.1016/j.measurement.2019.107295.

[7] A. Kusiak and Z. Zhang, "Analysis of Wind Turbine Vibrations Based on SCADA Data," *Journal of Solar Energy Engineering*, vol. 132, no. , Jun. 2010, Art. no. 031008, https://doi.org/10.1115/1.4001461.

[8] T. Wang, Q. Han, F. Chu, and Z. Feng, "Vibration based condition monitoring and fault diagnosis of wind turbine planetary gearbox: A review," *Mechanical Systems and Signal Processing*, vol. 126, pp. 662–685, Jul. 2019, https://doi.org/10.1016/j.ymssp.2019.02.051.

[9] S. Djurovic, C. J. Crabtree, P. J. Tavner, and A. C. Smith, "Condition monitoring of wind turbine induction generators with rotor electrical asymmetry," *IET Renewable Power Generation*, vol. 6, no. 4, pp. 207–216, Jul. 2012, https://doi.org/10.1049/iet-rpg.2011.0168.

[10] C. J. Crabtree, D. Zappalá, and P. J. Tavner, "Survey of commercially available condition monitoring systems for wind turbines," May 2014, [Online]. Available: https://durham-repository.worktribe.com/output/1632351.

[11] F. P. García Márquez, A. M. Tobias, J. M. Pinar Pérez, and M. Papaelias, "Condition monitoring of wind turbines: Techniques and methods," *Renewable Energy*, vol. 46, pp. 169–178, Oct. 2012, https://doi.org/10.1016/j.renene.2012.03.003.

[12] J. Fu, J. Chu, P. Guo, and Z. Chen, "Condition Monitoring of Wind Turbine Gearbox Bearing Based on Deep Learning Model," *IEEE Access*, vol. 7, pp. 57078–57087, 2019, https://doi.org/10.1109/ACCESS.2019.2912621.

[13] A. Kusiak and Z. Zhang, "Analysis of Wind Turbine Vibrations Based on SCADA Data," *Journal of Solar Energy Engineering*, vol. 132, no. 031008, Jun. 2010, https://doi.org/10.1115/1.4001461.

[14] X. Liu, J. Du, and Z.-S. Ye, "A Condition Monitoring and Fault Isolation System for Wind Turbine Based on SCADA Data," *IEEE Transactions on Industrial Informatics*, vol. 18, no. 2, pp. 986–995, Oct. 2022, https://doi.org/10.1109/TII.2021.3075239.